FISEVIER

Contents lists available at ScienceDirect

Chemical Engineering Journal

journal homepage: www.elsevier.com/locate/cej





Microfluidic-based platform for the semi-automated study of concentration, diffusion, and equilibrium binding of biomolecules

Adam K. Kowalski ^{a,b}, Tomasz Piros ^a, Slawomir Blonski ^c, Tetuko Kurniawan ^c, Piotr M. Korczyk ^c, Robert Hołyst ^a,

- ^a Institute of Physical Chemistry, Polish Academy of Sciences, Kasprzaka 44/52, 01-224 Warsaw, Poland
- b Institute for Molecules and Materials, Radboud University, Heyendaalseweg 135, 6525 AJ, Nijmegen, The Netherlands
- c Institute of Fundamental Technological Research, Polish Academy of Sciences, Pawinskiego 5B, 02-106 Warsaw, Poland

ARTICLE INFO

Keywords: Fluorescence correlation spectroscopy Microfluidies Biomolecular interactions Automation Diffusion coefficient Equilibrium constant

ABSTRACT

We introduce a novel microfluidic-based platform that automates single-molecule-sensitive measurements of biomolecular interactions using Fluorescence Correlation Spectroscopy (FCS) combined with FRET and Molecular Brightness Analysis (MBA). The developed system allows for the simultaneous analysis of biomolecule concentration, diffusion coefficient, and equilibrium constant in nanoliter-volume droplets. At the same time, it speeds up the measuring procedure by ~5 times compared to the standard one, reduces reactant consumption by ~2000 times compared to conventional cuvette-based FCS measurements, and limits the researcher's intervention to setting up the experiment and calibrating the microscope. We show the performance of the platform by studying DNA–DNA complex formation in response to ionic strength changes, as well as interactions of idarubicin with various nucleic acid complexes. The proposed solution paves the way for the automated optimization of non-covalent reaction conditions, leveraging non-invasive, high-precision statistical methods.

1. Introduction

DNA hybridization

Fluorescence Correlation Spectroscopy (FCS) is a highly sensitive single-molecule technique that enables the real-time investigation of molecular processes in solution. By analyzing fluorescence intensity fluctuations within a femtoliter-scale confocal volume, FCS provides quantitative information on molecular concentrations, diffusion coefficients, and hydrodynamic radii. Due to its high precision and low sample requirements, FCS has become a widely adopted method in molecular biology [1,2], biophysics [3], and pharmaceutical research [4, 5].

FCS can be combined with Förster Resonance Energy Transfer (FRET) – a method based on non-radiative energy transfer between two fluorescent molecules (donor and acceptor) – to enable the detection of molecular interactions within the 1–10 nm range. By titrating donor-and acceptor-labeled molecules and monitoring changes in FRET efficiency, an equilibrium binding constant (K) can be quantified and used to estimate interaction free energies. This approach has proven valuable for examining how molecular interactions respond to variations in pH [6], ionic strength [7], macromolecular crowding [8], or specific ion concentrations [9].

Similarly, FCS combined with Molecular Brightness Analysis (MBA) enables the determination of K without requiring dual labeling or energy transfer [10]. Instead, it leverages changes in the intrinsic fluorescence brightness of labeled molecules upon complex formation with non-fluorescent partners. These brightness variations result from steric shielding, charge transfer, or conformational rearrangements that alter the photophysical properties of the fluorophore. This approach has been successfully applied to study the binding of DNA to anthracyclines [11], oxazole dyes [12], and the influence of crowding on DNA hybridization [13].

Despite its strengths, FCS suffers from low throughput, particularly when applied to the determination of equilibrium binding constants via FRET or MBA. Reliable quantification typically requires 20–30 samples with varying biomolecular concentration ratios, each of which must be prepared and analyzed individually. This manual workflow is labor-intensive, time-consuming, and prone to pipetting errors, limiting the scalability of the method. While reducing the number of titration points may shorten the experiment, it compromises the accuracy of the equilibrium constant determination, as insufficient sampling of the transition region increases the fitting error.

E-mail addresses: akowalski@ichf.edu.pl (A.K. Kowalski), piotr.korczyk@ippt.pan.pl (P.M. Korczyk), rholyst@ichf.edu.pl (R. Hołyst).

Corresponding authors.

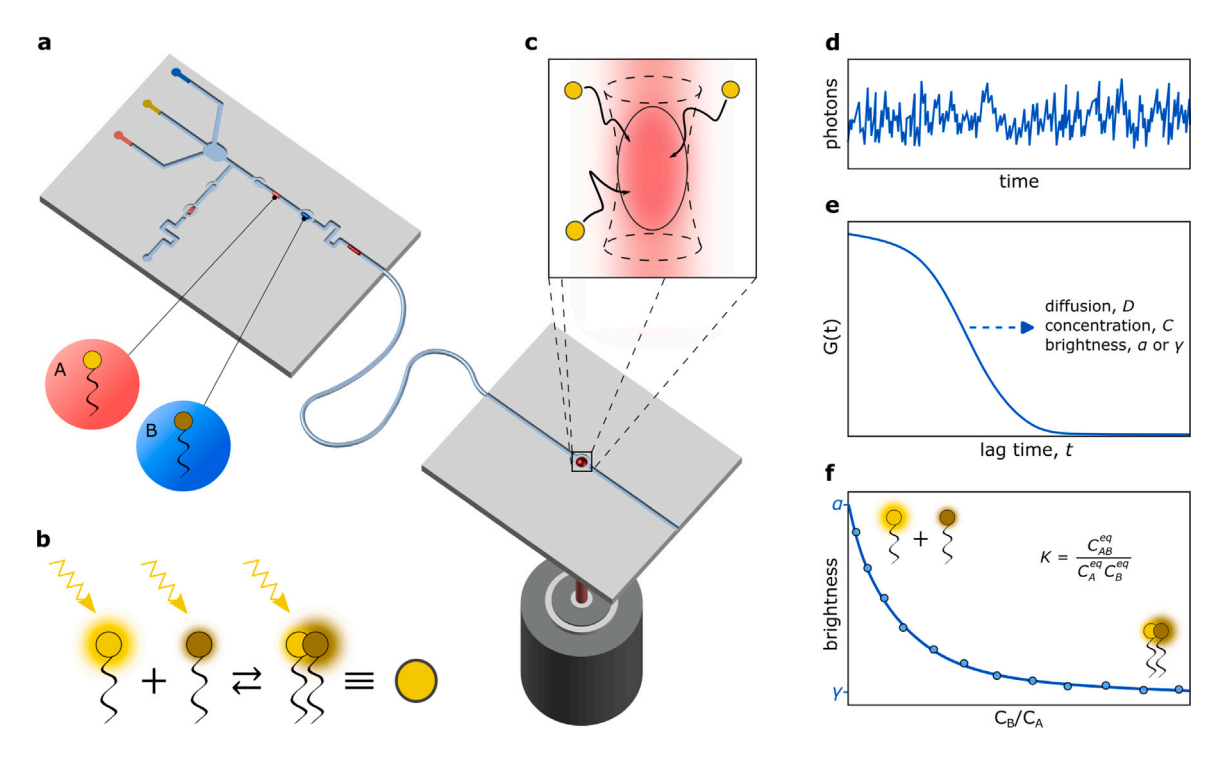


Fig. 1. Graphical representation of the system and measurements. We developed a microfluidic-based system for automated measurements of the equilibrium constant, diffusion coefficient, and concentration of fluorescent reactants. (a) The system generates a series of defined concentrations of reactants in droplets based on the geometries of hydrodynamic traps and sequencing procedures. Subsequently, droplets are transferred to the detection trap, where motion and interactions of reactants are investigated – (b) here, we study the hybridization of short DNA oligonucleotides labeling one or two strands with fluorescent dye. (c) Using confocal microscopy, we set the detection volume within a trapped droplet and (d) monitor fluorescence intensity fluctuations of reactants within it in time. (e) The autocorrelation function, $G(\tau)$, is fit by comparing these fluctuations in time, t, with fluctuations after lag time, $t + \tau$. As the result of fitting, the diffusion coefficient, concentration, and brightness of the reactant or mix of reactants are calculated. (f) By sampling a series of different reactant proportions, we monitor changes in brightness and quantify the equilibrium constant of DNA double-strand complex formation.

To overcome these limitations, we developed an integrated measurement platform that combines FCS with droplet-based microfluidics (Fig. 1). The system automates the sampling and measurement procedures, using previously designed hydrodynamic traps [14], and a modified droplet-generation system [15]. The key innovation of our setup lies in the implementation of a newly designed detection trap optimized for FCS measurements, as well as the integration of an automated nanoliter-scale dilution module compatible with FCS-FRET and FCS-MBA protocols. This design enables precise control over biomolecular concentrations and enhances the throughput of the measurements. Reagent consumption is reduced by three orders of magnitude to ~100 nL per droplet, while the time required for a single titration experiment is shortened from ~180 min to just 35 min. Following initial system calibration, the workflow proceeds with minimal user intervention, enabling fully automated titration experiments using programmable syringe pumps. Moreover, the system improves measurement reproducibility by minimizing user-dependent variability.

We demonstrate the utility of this platform by investigating (i) the influence of ionic strength on the stability of double-stranded DNA complexes and (ii) how parameters such as duplex length, AT/GC content, and nucleic acid type (DNA–DNA vs. DNA–RNA) affect the interaction of idarubicin with nucleic acids. Together, this platform integrates the precision of FCS with the efficiency of droplet microfluidics, enabling swift quantification of biomolecular interactions at nanomolar concentrations.

2. Results and discussion

2.1. Principles of the system operation

The developed system comprises three interconnected units: the Droplet On-Demand Unit (DODU), Detection Unit (DU), and Computation Unit (CU), as shown in Fig. 2a. DODU is responsible for generating

precise volume droplets and tuning reactant concentrations within them. DU traps droplets at designated spots and registers the fluorescent signals of reactants. Meanwhile, CU sets the dilution campaign, controls the flow of reactants based on image output from the camera, and analyzes the results.

The core of DODU is a microfluidic device that precisely manipulates single droplet concentration via droplet merging and splitting. The critical components of the device are microfluidic traps facilitating the fundamental manipulations of droplets. These traps, integrated into the microfluidic channel, affect droplet motion through bypass slits and obstacles that locally limit the lumen. As we described previously, by varying the dimensions of these elements, diverse functionalities of traps are achieved [14]. Here, we utilize two geometries for the concentration adjustment: the so-called metering (Fig. 2b left panel) and merging (Fig. 2b middle panel) traps.

The metering trap consists of an obstacle at one end, and its operation relies on the flow direction. The trap does not affect droplets entering from the obstacle side. However, it impacts the ones traveling in the reverse direction, immobilizing droplets shorter than the trap and dividing longer ones into two parts — one part being precisely the size of a trap and the second one of a remaining volume. The excess volume continues traversing downstream, and the metered portion can be released after another flow reversal. The formation of a droplet within a metering trap is depicted in Fig. 2c. For t_1 and t_2 , the flow of the aqueous phase goes downstream. As the liquid passes the obstacle, the flow is reversed (t_3 , t_4), and the droplet forms according to the geometry of the trap. Then, the flow direction inverts again (t_5), releasing the droplet. In the presented device, the metering traps generate single droplets of the input liquids and split the double-sized droplets into two droplets of uniform size.

On the other hand, the merging trap has barriers on both sides, immobilizing short droplets regardless of flow direction and passing

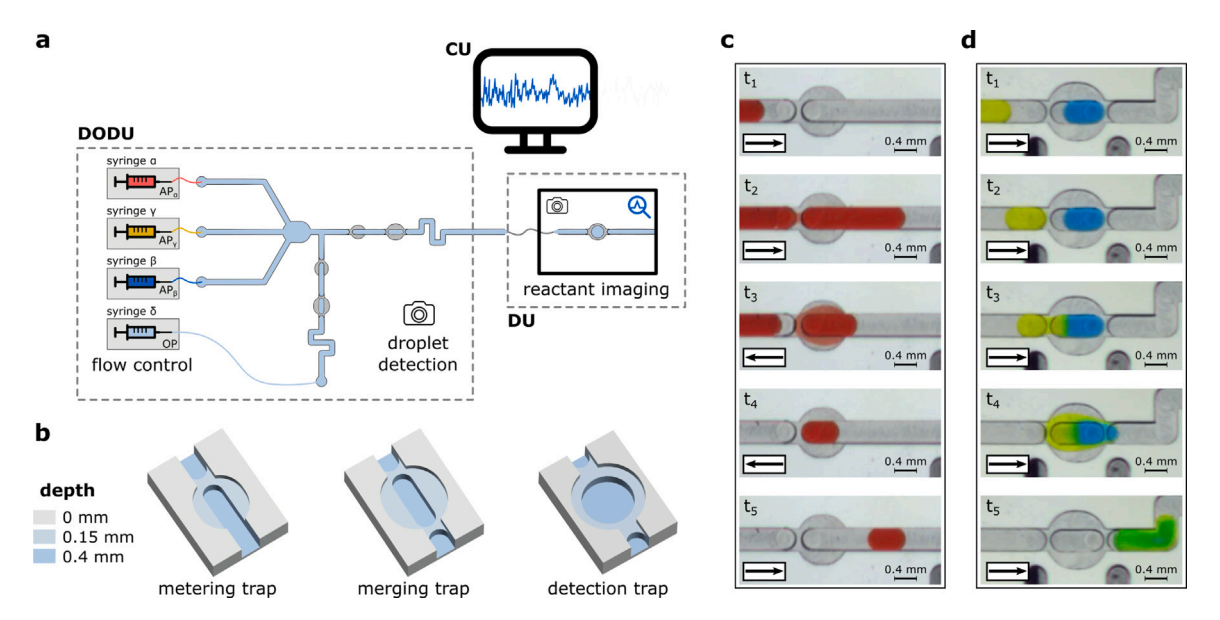


Fig. 2. The developed system and its components. (a) Representation of the system comprising Droplet On-Demand Unit (DODU), Detection Unit (DU), and Computation Unit (CU). (b) Precise geometries of hydrodynamic traps utilized in the cores of DODU and DU. The depths of geometries are depicted with various colors. (c, d) Experimental images in different instances illustrating the operation of (c) the metering trap and (d) the merging trap. Arrows indicate the directions of liquid flows.

longer ones unaffected. The different functionalities of the merging trap compared to the metering trap is caused by the geometry of the bypass slit and the speed of liquid flows. When two tiny droplets meet within the merging trap, they may either push each other out or coalesce, depending on the presence of an electromagnetic field (EMF). In the absence of EMF, droplets resist coalescence due to the energy barrier created by interfacial tension and the thin oil film between them. However, when EMF is applied, it induces changes in the charge distribution at the water/oil interface, reducing this barrier and enabling droplet merging. After the coalescence, the droplet is too long to be immobilized and exits the trap. This process is depicted in Fig. 2d, where two droplets generated by metering traps merge into a larger one. In our system, the merging traps are solely utilized to merge two single droplets of unit size into double-sized droplets with mixed content.

DODU consists of a microfluidic core operated by four bidirectional syringe pumps $(\alpha, \beta, \gamma, \text{ and } \delta)$ — each dedicated to a specific liquid, and a camera system for the registration of droplet movement. The core combines different arrangements of metering and merging traps distributed across two channels — Channel 1 and Channel 2. Unlike the previous system, where the entire mixing procedure occurred in one channel, this design separates the processes for increased efficiency and control [15]. The microfluidic core has three inlets for aqueous phases (AP) – AP_{α} , AP_{β} , AP_{γ} – followed by a dispensation chamber, two intersecting channels for droplet operations, and two outlets. Both channels have a similar pattern. Looking down the stream of AP, they consist of metering traps (1 and 2), merging traps (1 and 2), and geometry-inducing mixing of droplets (1 and 2), Fig. 3a. The channels differ only by the connection at the end. Channel 1 is linked to DU via tubing, while Channel 2 is bridged to the pump handling the oil phase flow (OP). Both metering traps are oriented with the barrier side towards the AP inlets, so the droplets form only when the flow is reversed. Additionally, metering traps are separated by a short canal with merging traps preventing the spontaneous formation of unwanted droplets. More precise models of DODU and DU cores are available in Supplementary Note S1.

The procedure for determining K using MBA involves mixing a reactant at a fixed concentration with a series of dilutions of a second reactant. Therefore, we utilized the first channel solely to dilute AP_{β} with AP_{γ} at various ratios, while the second one to mix AP_{α} with

diluted APB droplets. By processing output from the camera in realtime, CU manipulated flows in three directions: towards APs, OP, and the outlet, switching liquid flow directions according to the specific positions of droplets. The steps performed in the core of DODU are as follows. Syringe α dispenses AP_{α} into Channel 1, Fig. 3a. After AP_{α} passes Metering Trap 1, the flow in Syringe a reverses, producing an AP_{α} droplet, Fig. 3b. Then, Syringe δ dispenses oil to push the droplet to Merging Trap 1, Fig. 3c. Importantly, the flow of AP_{α} must be reversed before it enters the merging trap to avoid time discrepancies between system feedback and real-time positions of liquids. In the next step, Syringe β dispenses $AP_{\beta},$ and Syringe δ aspirates OP at the same flow rate, pushing AP_{β} into Channel 2, Fig. 3d. When AP_{β} passes Metering Trap 2, both syringes change the direction of piston motion, pushing back AP_{β} to form a droplet, Fig. 3e, and Syringe δ aspirates OP to move the AP_{β} droplet to Merging Trap 2, Fig. 3f. This procedure is repeated for AP,, Figs. 3g-i. However, when the AP, droplet enters Merging Trap 2, it coalesces with the APB droplet, and they traverse together through Mixing Canal 2. After mixing, the flow in Syringe β is reversed, splitting the double-sized droplet into two even halves while crossing Metering Trap 2, Fig. 3j. One half merges with AP_{α} , creating a blend of AP_{α} : AP_{β} : AP_{γ} in a 2:1:1 ratio, which flows to the DU, Fig. 3k. The other half returns to Merging Trap 2 for further operations, Fig. 3l. This cycle repeats, with each iteration (about one minute per interaction) forming and merging AP_{α} droplets with the AP_{β} and AP_{γ} blend at different ratios.

When the double-sized droplet forms, it exits DODU and enters DU via a long section of tubing (~180 cm of PTFE with 0.4 mm inner diameter). This length enables storage of the entire droplet series during generation and allows their subsequent transfer to the detection trap. The tubing can be smoothly detached from both units, enabling the storage of droplets, which is crucial for equilibrating specific reactants. However, since DNA double-stranded complexes and idarubicin–dsDNA complexes stabilize rapidly (within approximately 15 min and a few seconds, respectively — Supplementary Note S6) [16], the tubing is primarily used for droplet transfer between units to minimize data acquisition time. Importantly, all channels in the microfluidic cores of the DU and DODU, as well as the tubing interconnecting them, maintain the same diameter. This uniformity prevents droplet division at the junctions, securing consistent droplet integrity throughout the system.

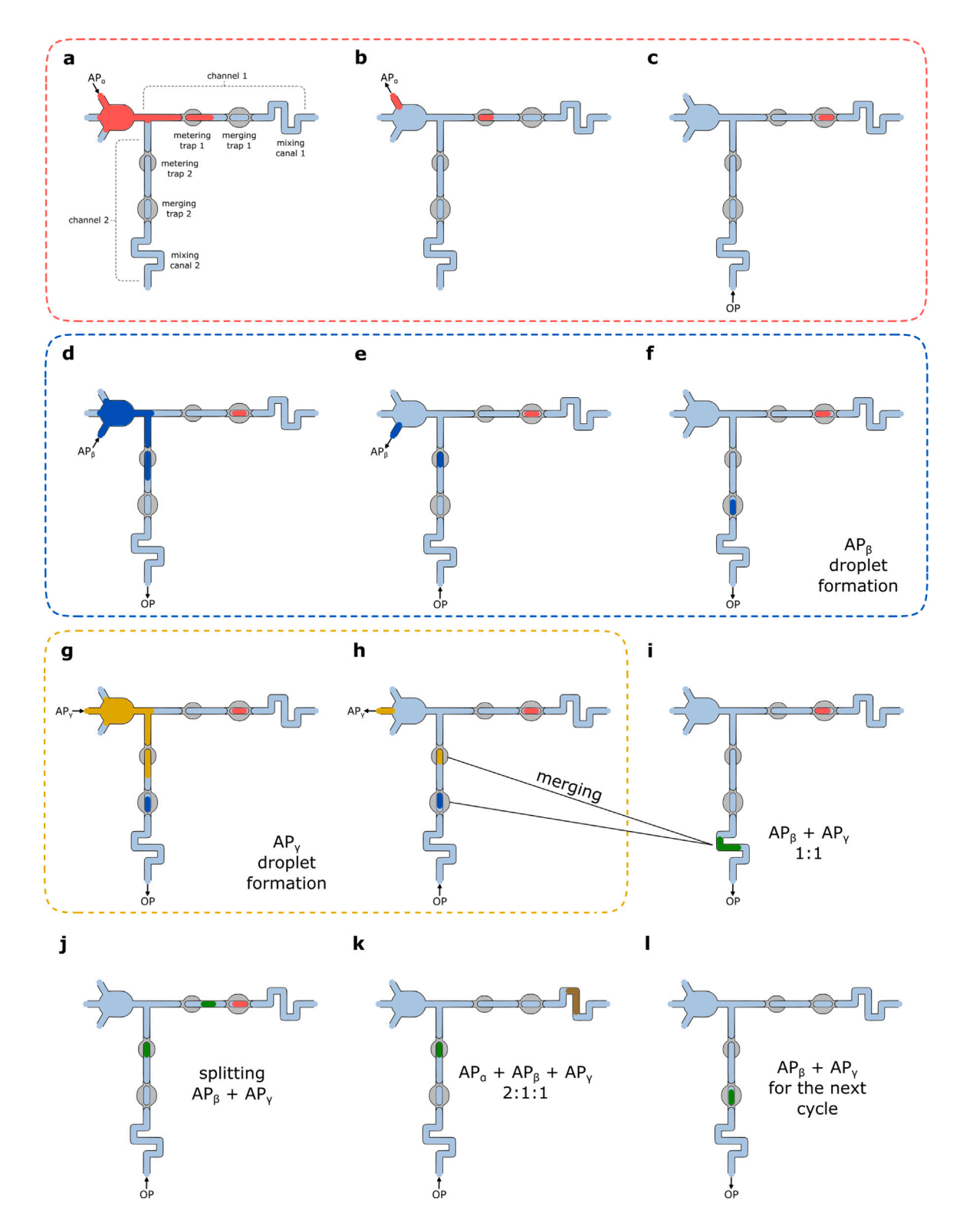


Fig. 3. Flow operations in one dilution cycle. (a–c) Formation of AP_{α} droplet. (d–i) Formation, mixing, and splitting of AP_{β} and AP_{γ} droplets. (j–l) Merging of AP_{α} with a blend of AP_{β} and AP_{γ} at a 2:1:1 ratio, respectively. Arrows indicate aqueous (AP) or oil (OP) phase flow directions for the specific interval of the cycle. (a) shows the notation used in the article.

DU consists of another microfluidic chip, a camera, and a confocal microscope equipped for FCS measurements. This microfluidic chip contains a single channel with the detection trap positioned in the middle and is connected to a waste reservoir at the outlet. Unlike metering and merging traps, the detection trap is a novel geometry

designed for the presented research to facilitate FCS measurements (Fig. 2b, right panel). It functions similarly to a merging trap by stopping droplets smaller than the trap size while allowing larger ones to pass. At the same time, it ensures a sufficient surface area for focal volume positioning within the immobilized droplets. Supplementary Video 1

shows the functioning of the detection trap during an exchange of blue and red droplets.

2.2. Image-based validation of droplet generation precision

The system validation involved generating a series of double-sized droplets (22 in total) by combining three food dyes introduced as AP_{α} – red, AP_{β} – blue, and AP_{γ} – yellow. In each droplet, AP_{α} consistently contributed half of the total volume, while AP_{β} and AP_{γ} were combined in varying ratios. The sequencing protocol for the AP_{β} and AP_{γ} blends is depicted in Supplementary Figure S2, while the entire dilution campaign is available in Supplementary Video 2.

To evaluate the reproducibility of the platform, we analyzed frames from Supplementary Video 2, extracting droplet contours at Metering Traps 1 and 2 and calculating their volumes, Fig. 4a. The method for estimating droplet volumes and the detailed results are provided in Supplementary Note S2.1. The average droplet volume at Metering Trap 1 was 97.62 \pm 0.30 nL, and at Metering Trap 2, 97.68 \pm 0.27 nL. The errors in droplet volume are weighted means calculated from the data in Supplementary Table S1. These results indicated excellent reproducibility of the metering traps and a strong consistency in droplet volumes across both traps, which encouraged us to proceed with the intended reactants.

2.3. Quantitative evaluation of DNA stability in aqueous droplets

After testing the operation of the microfluidic platform, we modified the APs and applied the system to confocal microscopy. AP_B and AP_y were replaced with 30 mM phosphate-buffered saline (PBS) containing red food dye to enhance visual properties. Meanwhile, AP_α consisted of the same solution but included a single-stranded DNA oligonucleotide tagged with a fluorescent dye. The food dye caused minimal background noise and slightly increased the diffusion coefficient of DNA, D_{DNA} , (from 127.00 \pm 2.16 μ m²/s to 136.33 \pm 1.25 μ m²/s) but did not affect the concentration of DNA, C_{DNA} (see Supplementary Figures S3b and S4). Most photons emitted by the food dye were reflected, preventing errors during platform validation. The spectra of the red food dye are shown in Supplementary Figure S3a. We monitored fluctuations in fluorescence intensity of diffusing DNA through a focal volume set within a droplet placed in the detection trap. Using the autocorrelation function, we compared fluorescence intensity fluctuations over time, f(t), with those after a lag time, $f(t+\tau)$, to obtain C_{DNA} , D_{DNA} , and brightness, α , of the reactant. Fig. 4b illustrates an example of the autocorrelation function fitted to the DNA signal in the droplet. In our experimental setup, the medium primarily consists of an aqueous PBS solution, supplemented with components present at very low concentrations (including Tween 20 below its CMC [17], and Allura Red dye at 0.01%), whose impact on the physical properties of the medium is minimal. The system is homogeneous at the molecular scale and lacks crowding or structural complexity. Therefore, the fluorescence intensity fluctuations were modeled using the standard 3D Brownian diffusion model [18,19].

To verify whether DNA remains in the aqueous phase and interacts with the surfactant at the PBS/oil interface, we generated a single droplet immersed in oil with surfactant and recorded C_{DNA} and D_{DNA} over five hours. Fig. 4c shows the reactant concentration within the droplet and the reactant diffusion coefficient — the data points correspond to FCS measurements available in Supplementary Figure S5. The constant C_{DNA} over time confirms stable DNA concentration within the droplet, while the constant D_{DNA} proves the stability of the reactant structure. Based on the average diffusion coefficient, we calculated the DNA hydrodynamic radius using the Stokes–Einstein equation – 1.71 \pm 0.05 nm – and compared it to the value from a control measurement – 1.74 \pm 0.02 nm – where the droplet had no contact with the oil phase; Supplementary Note S3.1. The matching sizes confirm no complex formation between DNA and the uncharged

surfactant present at the water/oil interface. Similar DNA behavior was observed with other uncharged surfactants in the previous study [16].

While the image analysis of tinted droplets provided valuable insights into droplet morphology, dye dispersion, and overall system operation, it lacked information on the distribution of biomolecule concentration across a series of dilutions. To fill this gap, we validated the system's functioning. We performed the same series of dilutions as in previous measurements and plotted the actual DNA concentration in droplets against the expected one (Fig. 4d; FCS measurements are available in Supplementary Figure S6). The data show an excellent alignment between predicted and actual concentrations, indicating high accuracy of the dilution procedure ($R^2 = 0.994$). Moreover, it confirms an even distribution of reactant concentration across the droplets after mixing, unaffected by the droplet movement.

2.4. Implementation of the system for determining equilibrium constants

Molecular Brightness Analysis (MBA) monitors changes in the count rate of a fluorescent reactant as the concentration of a second reactant increases. This results in a shift in fluorophore brightness as it binds to the other molecule, and K is calculated against reactant concentrations at equilibrium. A detailed description of MBA is provided in Supplementary Note S7.

K can be determined whether the second reactant is fluorescently labeled or not. When both reactants are labeled with fluorescent dyes and their spectra overlap, energy from one reactant (the donor) is transferred to the other (the acceptor) via dipole–dipole interactions, enhancing the brightness change of the reactants. Therefore, to test the platform's capabilities, we initially measured the equilibrium constant for DNA–DNA double-strand complex formation ($K_{DNA-DNA}$) by labeling both reactants with fluorescent dyes and using filters to monitor their brightness in two separate channels. The oligonucleotides were introduced in 30 mM PBS with red food dye to better distinguish the droplets from the oil phase. AP_{α} comprised the energy donor, AP_{β} the energy acceptor, and AP_{γ} was used as the diluting phase. Before the produced droplets entered DU, the full diluting campaign was completed, providing sufficient time (20 min) for the reactants to reach equilibrium (Supplementary Note S6).

 $K_{DNA-DNA}$ measured by the platform was $3.1 \cdot 10^8 \ \mathrm{M}^{-1} \pm 5.5\%$ (Fig. 4e red dashed line) and it overlapped with the one determined in the standard procedure, $2.8 \cdot 10^8 \ \mathrm{M}^{-1} \pm 7.0\%$ (Fig. 4e blue continuous line). The errors in $K_{DNA-DNA}$ were derived from the least-squares fit, while the count rate errors originated from the available instrumentation and sample preparation. The source data for Fig. 4e can be found in Supplementary Table S2. Both $K_{DNA-DNA}$ values were approximately one order of magnitude lower than the value reported by Bielec et al. $(3.6 \cdot 10^9 \ \mathrm{M}^{-1})$ for a comparable system [20]. In our experiments, however, the measurements were carried out in 30 mM PBS containing red food dye. We verified that the dye was responsible for the discrepancy: repeating the experiment in 30 mM PBS without dye yielded $K_{DNA-DNA} = 5.3 \cdot 10^9 \ \mathrm{M}^{-1}$ (Supplementary Note S3.2), consistent with Bielec et al. and slightly higher due to the increased ionic strength.

2.5. Application of the system for investigating biomolecular interactions

2.5.1. DNA-DNA interactions in PBS solutions of varying concentrations

With a fully functioning system, we replaced the fluorescent acceptor with its non-fluorescent analog, removed the food dye to avoid additional dye-reactant interactions, and investigated DNA-DNA complex formation in relation to PBS concentration. The change in $K_{DNA-DNA}$ versus the ionic strength (I) is presented in Fig. 5b, including errors derived from the least-squares fit. I was calculated using equation:

$$I = \frac{1}{2} \sum_{i=1}^{n} c_i z_i^2,\tag{1}$$

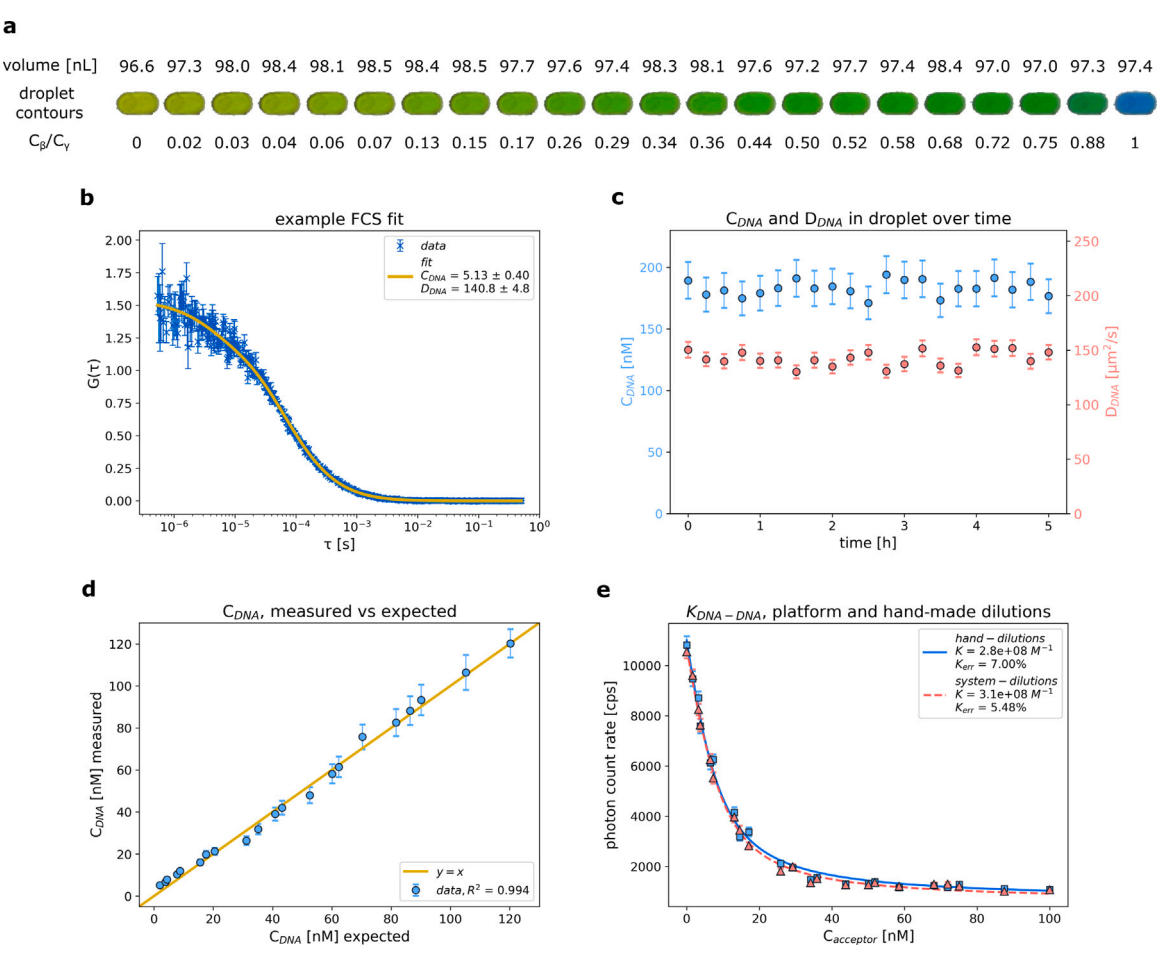


Fig. 4. System validation. (a) Validation of the dilution protocol and droplet volumes. The presented droplets are the snapshots taken by the camera in Metering Trap 2, showing the increase in AP_β content. (b) An example of a single FCS measurement in a nanoliter droplet, where τ is the lag time and $G(\tau)$ is the autocorrelation function of the fluorescence intensity fluctuations. (c) Constant concentration, and diffusion coefficient of DNA in time within a single droplet positioned in the detection trap. (d) The expected versus measured concentration of DNA in droplets — dilutions performed by the platform. (e) The equilibrium constant of the DNA–DNA hybridization reaction ($K_{DNA-DNA}$) determined by hand-made dilutions and by the platform. FRET donor concentration was kept constant, while FRET acceptor concentration ($C_{acceptor}$) varied (x-axis). The y-axis represents the photon count rate (counts per second, cps), corresponding to specific acceptor/donor ratios.

where C_i is the concentration of ion i, and z_i is the charge number of that ion. The corresponding $K_{DNA-DNA}$ fits and source data are provided in Supplementary Note S4.

As more ions are added to the solution, $K_{DNA-DNA}$ increases by more than 3 orders of magnitude from $3.6 \cdot 10^6 \text{ M}^{-1}$ for 5 mM PBS to $8.0 \cdot 10^9$ M⁻¹ for 150 mM PBS, similarly to previous studies [13]. This increase is due to reduced electrostatic repulsion between the negatively charged DNA strands. Higher ionic strength enhances charge screening over short distances, thereby stabilizing the DNA duplex [21]. Consequently, the Debye length, which represents the effective range of electrostatic interactions in solution, decreases, reaching a plateau at salt concentrations above 100 mM. The anomalous increase in screening length observed in some studies was not detected here, as the reaction was not examined at higher PBS concentrations (~1 M) [22]. Furthermore, single-molecule studies have shown that increased ionic strength enhances the association rates of DNA hybridization while having minimal impact on dissociation rates [23]. These findings suggest that higher ionic environments promote the formation of DNA duplexes without significantly altering their stability once formed.

It should be noted that the absolute values of $K_{DNA-DNA}$ determined here (single-labeled system) differ from those reported in Section 2.4 (double-labeled system). When both strands carry fluorophores at the same end, additional π - π stacking interactions between dyes can stabilize the duplex and increase the apparent affinity by up

to an order of magnitude [10]. This effect explains why $K_{DNA-DNA}$ in Section 2.4 reached $5.3 \cdot 10^9 \, \mathrm{M}^{-1}$, while the single-labeled system used here yielded lower values at comparable ionic strength. We emphasize that this discrepancy arises from the labeling strategy rather than from inconsistencies in the measurement platform.

2.5.2. Interactions of idarubicin with various nucleic acid complexes

As a second example of our platform application, we studied the interactions of idarubicin (IDA) with various double-stranded nucleic acid complexes (dsNA), including DNA–DNA duplexes, DNA–RNA hybrids of varying lengths (10, 20, and 30 bp), and homopolymeric sequences such as poly(AT) and poly(GC). The equilibrium constant of IDA-dsNA complex formation ($K_{IDA-dsNA}$) was measured in 100 mM sodium phosphate buffer (PB-NA+ at pH 7.4 containing 0.002% Tween 20. The concentration of IDA was fixed at 40 nM, while the concentration of dsNA duplexes was varied from 0 to 100 nM, using the same serial dilution protocol as described earlier (Supplementary Note S2). Owing to the rapid equilibration of IDA-dsNA complexes (within a few seconds, Supplementary Note S6), the entire droplet series was transferred to the detection chamber without additional incubation (it takes ~20 min to complete a series of droplets).

IDA, a planar anthracycline molecule, binds to dsNA via a two-step mechanism (Fig. 5a). At low molar ratios ($C_{IDA}/C_{dsNA} < 0.3$), IDA intercalates between base pairs of the duplex through π - π stacking

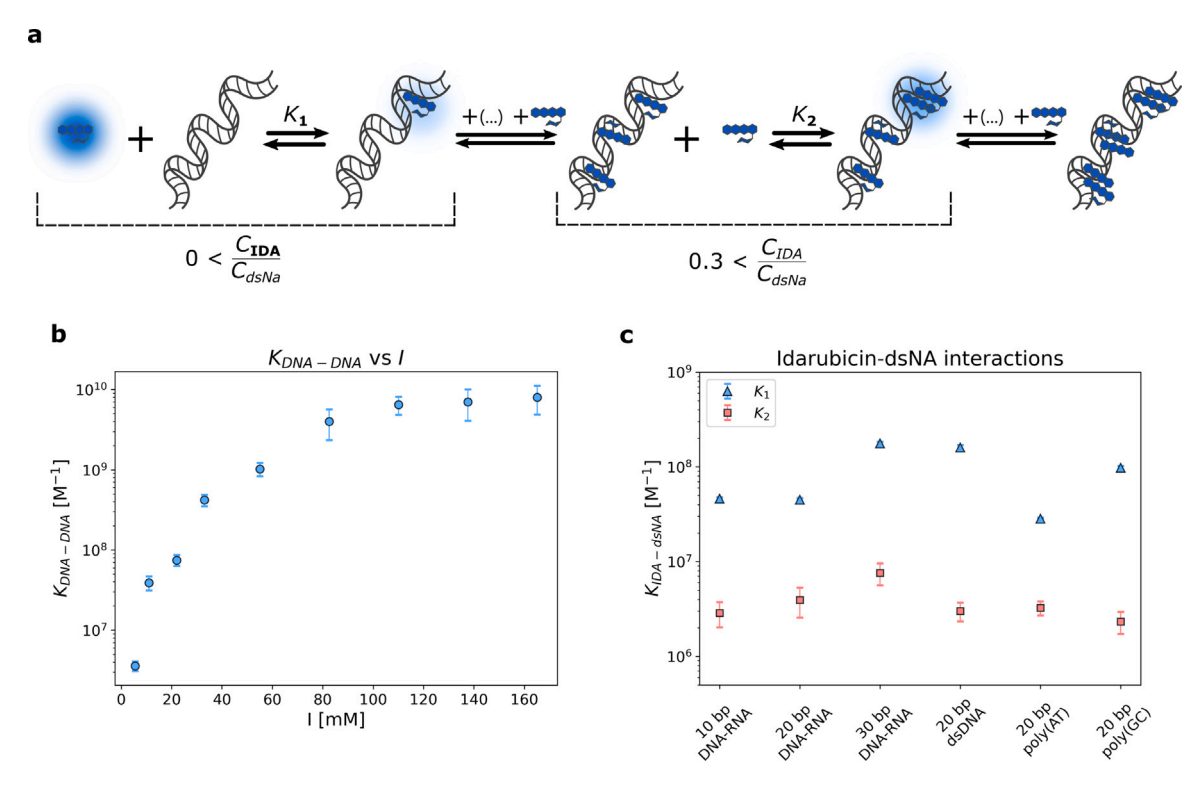


Fig. 5. Application of the system for studying DNA–DNA and idarubicin–dsNA interactions. (a) Schematic representation of the two-step binding mechanism of idarubicin (IDA) with double-stranded nucleic acid complex (dsNA). At low IDA/dsNA ratios (<0.3), IDA intercalates between nucleic acid base pairs, forming high-affinity complexes governed by equilibrium constant K_1 , which results in strong fluorescence quenching due to restricted chromophore rotation. As DNA binding sites become saturated ($C_{IDA}/C_{dsNA} > 0.3$), excess IDA associates with preformed IDA-dsNA complexes through electrostatic interactions (K_2), resulting in multimeric assemblies. In this regime, fluorescence quenching is less pronounced, as the chromophore remains partially mobile. **(b)** Equilibrium constant of DNA–DNA interactions ($K_{DNA-DNA}$) as a function of ionic strength (I). **(c)** Equilibrium constants of idarubicin binding to double-stranded nucleic acid complexes ($K_{IDA-dsNA}$). K_1 corresponds to high-affinity intercalation of IDA into dsNA, while K_2 reflects the subsequent, lower-affinity association of free IDA with preformed IDA-dsNA complexes.

interactions. This process yields high-affinity complexes characterized by equilibrium constant K_1 and results in pronounced fluorescence quenching due to restricted idarubicin rotation. Once the available intercalation sites become saturated, excess IDA binds externally to the preformed IDA-dsNA complexes via electrostatic interactions, forming multimeric assemblies. This secondary binding step is governed by a weaker equilibrium constant K_2 and exhibits substantially less fluorescence quenching because the chromophore remains partially mobile. These two regimes can be distinguished by monitoring molecular brightness as a function of C_{IDA}/C_{dsNA} , showing a sharp transition at a ratio of approximately 0.3 [11].

We observed that K_1 values varied from $2.9 \cdot 10^7$ to $1.8 \cdot 10^8$ M⁻¹ depending on duplex type (Fig. 5c). The corresponding $K_{IDA-dsNA}$ fits and source data are provided in Supplementary Note S5. The highest K_1 was recorded for 30 bp DNA-RNA hybrids, consistent with the principle of cooperative intercalation: as the helix length increases, π - π stacking interactions stabilize drug binding [24]. In contrast, homopolymeric poly(AT) sequences showed substantially reduced affinity compared to poly(GC), confirming prior observations that IDA preferentially intercalates into GC-rich sequences [25]. For direct comparison, K_1 for the IDA-dsDNA complex was $1.6 \cdot 10^8$ M⁻¹, while for the IDA-DNA-RNA hybrid it was $4.5 \cdot 10^7$ M⁻¹, indicating stronger binding to canonical dsDNA. This observation is consistent with previous reports that idarubicin exhibits higher affinity and more stable intercalative binding to double-stranded DNA, whereas its interactions with RNA or DNA-RNA hybrids are comparatively weaker and mediated by mixed binding modes, including groove binding and hydrogen bonding [26-28].

The secondary equilibrium constant K_2 was consistently an order of magnitude lower than K_1 (typically $\sim 3 \cdot 10^6 \, \mathrm{M}^{-1}$), with only slight variation across sequence types, reflecting the nonspecific nature of the

electrostatic interaction. Our results are in good agreement with recent brightness-based studies by Zhou et al. who reported two-step binding mechanisms for various anthracyclines, including idarubicin [11]. Their measured K_1 and K_2 for IDA with 69 bp dsDNA were $5 \cdot 10^7 \ \mathrm{M}^{-1}$ and $2 \cdot 10^6 \ \mathrm{M}^{-1}$, respectively, and closely matched our results, despite minor distinctions in experimental setup.

2.6. Comparing manual and automated workflows

The standard procedure for determining a single *K* value in a specific solution involves the following steps: (i) calibration of the confocal microscope, (ii) preparation of stock solutions, (iii) performing consecutive dilutions, (iv) mixing samples, (v) waiting for equilibrium to be established (vi) transferring solutions to plates dedicated to confocal microscopy, (vii) conducting measurements, and (viii) analyzing results. Steps (iii) and (iv) for 20 samples typically require approximately one hour, while steps (vi) and (vii) take about two hours. During these steps, the operator performs all tasks manually. Notably, step (vi) involves solely moving the stage in the x, y, and z coordinates to set the focal volume within each specific sample and pressing the measurement button. This process is repeated 20 times for individual measurements.

The developed system automates steps (iii–iv) and (vi–vii), significantly reducing operator workload. Specifically, automation saves approximately three hours of operator time when determining a single K value. For more complex studies, such as those detailed in Sections 2.5.1 and 2.5.2, the system saved 27 h (for nine measured K values) and 18 h (for six measured K values) of operator time, respectively. Simultaneously, the system completed the measurements in 5.5 and 3.5 h for these cases, respectively. The discrepancy between

the operator time saved and the total duration required by the automated platform to complete the measurements arises from several factors. These include eliminating the need to adjust the focal volume between plate wells manually, the removal of plate exchange steps, and reducing the time required for sample dilutions. This automation not only improves efficiency but also reduces the potential for human error during repetitive tasks, enhancing the overall reliability of the measurement process.

Additionally, the standard protocol typically relies on disposable 8-well plates, which accommodate 200 μL of solution per well. Other commonly used formats include 24-, 96-, and 384-well plates. In the case of 384-well plates, the working volume is reduced to approximately 30 μL per well. However, the high number of wells can hinder sample access and markedly prolong measurement times. In contrast, our platform employs a reusable detection unit with nanoliter droplets (100 nL) separated by oil, which significantly reduces reagent consumption and eliminates the need for conventional well plates, providing a more sustainable and efficient approach.

It should be noted that the initial setup of the automated platform requires additional preparation compared to conventional manual workflows. This includes connecting the syringe pumps, sealing the PTFE tubings, assembling the microfluidic units, and aligning the detection trap with the confocal microscope. These steps are relatively complex and require some operator training, but they are one-time efforts. Once completed, the platform runs stably and reproducibly, enabling subsequent experiments to proceed with minimal user intervention. Thus, while the initial system integration is more demanding than standard sample pipetting, the long-term benefits in reproducibility, reagent economy, and operator time savings outweigh the initial complexity.

3. Conclusions

The developed microfluidic-based platform offers a significant advancement in the precise measurement of parameters such as concentration, diffusion coefficient, and equilibrium constant of molecules at nanomolar concentrations. By integrating FCS-FRET and FCS-MBA with a microfluidic system, the platform automates the process of K measurements. It cuts reagent usage by a factor of 2000 compared to conventional cuvette-based FCS measurements and significantly reduces the need for human involvement, which boosts the precision and consistency of the results.

In this work, we kept the constant concentration of AP_{α} in the droplets. However, the platform might as well be utilized to vary the concentration of all phases. Moreover, one might access unlimited mixing configurations of multiple reactants by tuning flows of liquids and applying other hydrodynamic traps [14]. Although increasing the throughput of FCS was not the primary goal of our project, the architecture we implemented allows for moderate scalability — primarily by reducing the need to navigate the three-dimensional space of the sample and enabling the incorporation of parallel measurement lines. The compact size of the platform makes it well-suited for future expansion, including the addition of new modules, integration with other analytical techniques, or enhancement of its functional capabilities.

Automation is a key element in the further development of our system. Thanks to its open architecture, the platform supports not only the integration of additional pumps or measurement sequences but also the implementation of advanced sequential logic to droplet microfluidics [29]. Such adaptive feedback could enable dynamic optimization of reaction conditions, helping to overcome the limited throughput of conventional FCS while preserving its precision and sensitivity.

As such, our system represents a step towards automated, precise, and versatile molecular measurements — bridging the strengths of microfluidic and correlation-based techniques. As a result, it broadens the potential applications of the system, including: (i) studying biomolecular interactions where weak non-covalent forces are pivotal, such as in

drug–DNA interactions, protein-protein binding, and enzyme kinetics; (ii) facilitating early-stage screening and characterization of potential therapeutic compounds in drug development; and (iii) enabling rapid and sensitive detection of biomarkers in diagnostics.

4. Materials and methods

4.1. Liquids and reactants

Novec 7500 (3M, USA) with 2% fluorosurfactant (RAN Biotechnologies, USA) was used as OP in all measurements. The surfactant sustains stable aqueous droplets and prevents them from wetting the channel walls. To visualize the operation of DODU core, we introduced Mili-Q water with food dyes, i.e., $AP_{\alpha}-0.01\%$ Allura Red AC (E129), $AP_{\beta}-0.1\%$ Brilliant Blue FCF (E133), and $AP_{\gamma}-0.1\%$ Quinoline Yellow WS (E104).

4.1.1. Measurements of C_{DNA} , D_{DNA} , and $K_{DNA-DNA}$

In the experiments described in Sections 2.3, 2.4, and 2.5.1, we used 20-nucleotide single-stranded DNA oligonucleotides (IDT, USA) as reactants. The oligonucleotides were stored at $-20\,^{\circ}\mathrm{C}$ in standard Tris-EDTA buffer as 100 μM stock solutions. Prior to measurements, DNA strands were diluted in phosphate-buffered saline (PBS) pH 7.4 containing 0.002% Tween 20 to minimize adsorption to vial walls and air–liquid interfaces during sample preparation [20]. All measurements were performed at 25 $^{\circ}\mathrm{C}$.

- (i) In Section 2.3, we studied a single DNA strand labeled with Atto488 at varying concentrations (Atto488 5' ATCGTTGGAGCTTGAGGCAT 3') in 30 mM PBS supplemented with 0.01% Allura Red AC (E129).
- (ii) In Section 2.4, we used a pair of complementary oligonucleotides labeled at the same end with Atto488 and Atto647N, respectively (Atto488 5' ATCGTTGGAGCTTGAGGCAT 3' and 5' ATGCCTCAA-GCTCCAACGAT 3' Atto647). The concentration of the donorlabeled strand was fixed at 10 nM, while the concentration of the acceptor-labeled strand was varied from 0 to 100 nM according to the serial dilution protocol described in Supplementary Note S2. The measurements were performed in 30 mM PBS supplemented with 0.01% Allura Red AC (E129).
- (iii) In Section 2.5.1, the donor strand was labeled with Atto488 (Atto488 5' ATCGTTGGAGCTTGAGGCAT 3') and the complementary strand was non-fluorescent (5' ATGCCTCAAGCTCCAACGAT 3'). Again, the concentration of the labeled strand was fixed at 10 nM, and the concentration of the unlabeled strand was varied from 0 to 100 nM following the same serial dilution protocol as in (ii). The measurements were performed in various concentrations of PBS (no food dye).

4.1.2. Measurements of idarubicin-dsNA interactions

To investigate the effect of various nucleic acid duplexes on idarubicin binding, we used a set of synthetic single-stranded oligonucleotides purchased from Genomed (Poland). The sequences included: DNA: 5' ATCGTTGGAGCTTGAGGCAT 3', RNA: 5' AUCGUUGGAGCU-UGAGGCAU 3', DNA: 5' ATCGTGGCAT 3', RNA: 5' AUGCCACGAU 3', DNA: 5' GCATCTGTCATCGTGTAGGCATCGTAGGTA 3', RNA: 5' UACCUACGAUGCCUACACGAUGACAGAUGC Additionally, 20-nucleotide poly(A), poly(T), poly(G), and poly(C) sequences were used to form complementary duplexes. Single strands were diluted in Tris-EDTA buffer to a concentration of 100 µM. Complementary sequences were mixed to allow duplexes formation: poly(AT), poly(GC), 20 bp DNA-DNA, and DNA-RNA hybrids of lengths 10 bp, 20 bp, and 30 bp. These duplexes were stored as 50 µM stock solutions at -20 °C (DNA-DNA complexes) or -80 °C (DNA-RNA complexes). Idarubicin hydrochloride (purchased from United States Pharmacopeia (USP), USA) was dissolved in Milli-Q water to prepare a 1 mM stock solution, stored at 4 $^{\circ}$ C. For all further dilutions of both idarubicin and nucleic acid duplexes, phosphate buffer with sodium ions (PB–Na⁺, 100 mM, pH = 7.4), supplemented with 0.002% Tween 20 and 1 mM EDTA, was used.

4.2. Droplet on-demand unit

The system was fabricated utilizing a CNC milling machine (Ergwind, Poland) equipped with a 0.4 mm end mill (FR208, inGraph, Poland). The geometries were engraved in one 4 mm polycarbonate plate (Makrolon, Bayer AG, Germany); see Supplementary Figure S1. The second – 4 mm PC plate with holes for inlets and an outlet – was bonded to seal the channels. To position plates correctly, we inserted steel pins of 0.8 mm diameter into ancillary holes and merged them using a hot press at 135 °C and 2 bars for 15 min. Subsequently, we modified the channels introducing Novec 1720 (3M, USA) at 15 millibars for 2 min and inserted the device into the oven at 90 °C for 15 min. To ensure proper droplet coalescence, we applied an electromagnetic field by infixing wire electrodes (UL3239 28AWG with insulation XLPE, rated voltage 6 kV-DC) into dedicated channels. The APs and OP were introduced via PTFE tubings (Bola GmbH, Germany) flattened at the end and sealed with PC plate by 1.2 mm diameter screws with nuts. The outlet Teflon tubing of 0.4 mm diameter was fastened in the same manner. After each droplet generation, the channels were filled with OP.

4.3. Detection unit

The system comprised a polydimethylsiloxane (PDMS) part with pocket channels - P1 - bounded to 0.1 mm microscope cover glass (ESCO, USA) - P2. The detection system was connected to DODU at the inlet and to the waste at the outlet with PTFE tubing of 0.4 mm inner diameter and 0.9 outer diameter (Bola GmbH, Germany). P1 was cast by adding the blend of 10:1 ratio of PDMS base (Sylgard, USA) and curing agent (Sylgard, USA) into the negative mold and curing it at 75 °C for 3 h, similarly to Friend and Yeo protocol [30]. Next, P1 was removed from the negative mold and exposed with P2 for 1 min to oxygen plasma in plasma cleaner (Harrick Plasma, USA). The negative mold was prepared by pouring the same blend as for P1 over the polycarbonate mask and curing it under the same conditions as P1. Additionally, the negative mold was silanized with (3-Aminopropyl)triethoxysilane (Sigma-Aldrich, USA) vapor in the vacuum chamber at 10 millibars for 1 h before casting P1. The mask was fabricated using a CNC milling machine (Ergwind, Poland) equipped with a 0.4 mm endmill (FR208, inGraph, Poland) in a 4 mm polycarbonate plate (Makrolon, Bayer AG, Germany). The flow of droplets into DU was monitored with UI-3274LE-C-HQ CCD camera (IDS, Germany).

4.4. Microfluidic setup

To control fluid motion, we utilized the low-pressure Nemesys 290 N syringe pumps (Cetoni GmbH, Germany) conjugated with HSZ-645TR stereoscope (Huvitz, South Korea) and UI-3274LE-C-HQ CCD camera (IDS, Germany). The OP and APs were introduced into 1 ml glass syringes (Hamilton, USA) connected to DODU via PTFE tubings (Bola GmbH, Germany) of 0.8 mm inner diameter and 1.6 mm outer diameter. The droplet formation was regulated by the self-written Python script applying the feedback from the real-time image to four pumps (three for various APs and one for OP). The automated procedure prevented undesirable mixing of APs that could occur due to liquid leakage at interconnections and maintained fixed distances between consecutive droplets.

4.5. Microscope setup

Reactant properties and interactions were gauged on a Nikon C1 inverted confocal microscope with the PicoQuant LSM module supported with the PicoHarp 300 Time-Correlated Single-Photon Counting setup (TCSPC). The samples were measured directly in droplets trapped in the core of detection unit. The DU core was placed over the objective, and the focal volume parameters were set using a Nikon PlanApo water immersion lens $60 \times (NA = 1.2)$. The focal volume was positioned 10 μm from the glass bottom and kept still during droplet exchange. We estimated the size of the focal volume by calibrating the system with Rhodamine 110 (Sigma-Aldrich, USA) and performing the FCS measurements. To excite samples, we used a pulsed diode laser with pulsed interval excitation emitting photons of two wavelengths (485 nm and 636 nm) in intervals (PicoQuant GmbH, Germany). The pulse frequency was 40 MHz, and the optimized laser power was 40 μ W or 50 μ W for idarubicin interactions (power meter PM 100, Thorlabs, measured at a position in front of the light entering the objective). For the double labeled system we registered data in two different channels and used a dichroic mirror T635. In the first channel (CH1), we monitored the fluctuations in fluorescence intensity coming after the pulse of the 485 nm laser, and in the second channel (CH2), after the 636 nm one. The shaded climate chamber (OkoLab, Italy) covered the measurement setup to prevent noise detection and maintain the constant temperature of 25 °C. The signal was collected by a single-photon avalanche photodiode (PerkinElmer Optoelectronics, Canada) after transmission through the 645 long-pass filter for CH2 and the 525/50 filter for CH1. The acquired data was analyzed using the self-written Python script, while the microscope setup was controlled with the PicoQuant Sepia II laser controller and the SymphoTime 64 software. In the case of single-labeled system we recorded photons only in one channel using the 485 nm laser, 488 long-pass filter, and the same laser power and pulse frequency.

CRediT authorship contribution statement

Adam K. Kowalski: Writing – review & editing, Writing – original draft, Visualization, Validation, Software, Methodology, Investigation, Formal analysis, Data curation, Conceptualization. Tomasz Piros: Writing – review & editing, Methodology, Investigation. Slawomir Blonski: Supervision, Resources, Methodology. Tetuko Kurniawan: Methodology, Investigation. Piotr M. Korczyk: Writing – review & editing, Supervision, Resources, Funding acquisition. Robert Holyst: Writing – review & editing, Validation, Supervision, Resources, Project administration, Formal analysis.

Declaration of competing interest

The authors declare that they have no known competing financial interests or personal relationships that could have appeared to influence the work reported in this paper.

Acknowledgments

This work was supported by the National Science Centre, Poland, within the grant Preludium Bis 2 no. 2020/39/O/ST4/00877. A.K.K. was supported by the Foundation for Polish Science (FNP). P.M.K. acknowledges support from First Team grant (POIR.04.04. 00-00-3FEF/17-00) of the Foundation for Polish Science, co-financed by the EU under the Smart Growth Operational Program and the National Science Centre, Poland, under grant OPUS no. 2023/51/B/NZ6/02951.

Appendix A. Supplementary data

The supplementary information includes the following: (i) a more detailed platform design, (ii) the dilution procedure, (iii) the method for calculating droplet volumes, (iv) fluorescence spectra of Allura Red food dye, (v) FCS background noise, (vi) FCS measurements of ssDNA in PBS or PBS with Allura Red food dye, (vii) source data for ssDNA FCS measurements in a single droplet over time, (viii) source data for ssDNA FCS measurements in droplets across a series of dilutions, (ix) source data for count rate and error values of $K_{DNA-DNA}$ prepared by the platform and by a human, (x) a comparison of ssDNA size measured in droplets versus in solution, (xi) fits and values of $K_{DNA-DNA}$ constants versus ionic strength, (xii) fits and values of $K_{IDA-dsNA}$ constants for various nucleic acid complexes, (xiii) association rates of studied biomolecule complexes and (xiv) Molecular Brightness Analysis method for the determination of equilibrium constants.

Supplementary material related to this article can be found online at https://doi.org/10.1016/j.cej.2025.169512.

Data availability

Data will be made available on request.

References

- K. Tsekouras, A.P. Siegel, R.N. Day, S. Pressé, Inferring diffusion dynamics from FCS in heterogeneous nuclear environments, Biophys. J. 109 (2015) 7–17, http://dx.doi.org/10.1016/j.bpj.2015.05.035.
- [2] F. Schneider, D. Waithe, M.P. Clausen, S. Galiani, T. Koller, G. Ozhan, C. Eggeling, E. Sezgin, Diffusion of lipids and GPI-anchored proteins in actin-free plasma membrane vesicles measured by STED-FCS, Mol. Biol. Cell 28 (2017) 1507–1518, http://dx.doi.org/10.1091/mbc.e16-07-0536.
- [3] A. Khmelinskaia, J. Mücksch, F. Conci, G. Chwastek, P. Schwille, FCS analysis of protein mobility on lipid monolayers, Biophys. J. 114 (2018) 2444–2454, http://dx.doi.org/10.1016/j.bpj.2018.02.031.
- [4] R. Zhao, H. Zheng, Z. Zhong, C. Zhao, Y. Sun, Y. Huang, X. Zheng, Efficient removal of diclofenac from surface water by the functionalized multilayer magnetic adsorbent: Kinetics and mechanism, Sci. Total. Env. 760 (2021) 144307, http://dx.doi.org/10.1016/j.scitotenv.2020.144307.
- [5] J. Sankaran, T. Wohland, Current capabilities and future perspectives of FCS: Super-resolution microscopy, machine learning, and in vivo applications, Commun. Biol. 6 (2023) 699, http://dx.doi.org/10.1038/s42003-023-05069-6.
- [6] H. Chen, F. Ding, Z. Zhou, X. He, J. Shen, FRET-based sensor for visualizing pH variation with colorimetric/ratiometric strategy and application for bioimaging in living cells, bacteria and zebrafish, Anal. 145 (2020) 4283–4294, http://dx.doi.org/10.1039/D0AN00841A.
- [7] B. Liu, B. Poolman, A.J. Boersma, Ionic strength sensing in living cells, ACS Chem. Biol. 12 (2017) 2510–2514, http://dx.doi.org/10.1021/acschembio. 7b00348.
- [8] A.J. Boersma, B. Liu, B. Poolman, A sensor for quantification of macromolecular crowding in living cells, Biophys. J. 108 (2015) 114a, http://dx.doi.org/10.1038/ nmeth.3257.
- [9] Y. Shen, S.-Y. Wu, V. Rancic, A. Aggarwal, Y. Qian, S.-I. Miyashita, K. Ballanyi, R.E. Campbell, M. Dong, Genetically encoded fluorescent indicators for imaging intracellular potassium ion concentration, Commun. Biol. 2 (2019) 18, http: //dx.doi.org/10.1038/s42003-018-0269-2.
- [10] K. Bielec, G. Bubak, T. Kalwarczyk, R. Hołyst, Analysis of brightness of a single fluorophore for quantitative characterization of biochemical reactions, J. Phys. Chem. B 124 (2020) 1941–1948, http://dx.doi.org/10.1021/acs.jpcb.0c00770.
- [11] Y. Zhou, K. Bielec, P. Pasitsuparoad, R. Holyst, Single-molecule brightness analysis for the determination of anticancer drug interactions with DNA, Anal. 145 (2020) 6600–6606, http://dx.doi.org/10.1039/D0AN01108H.

- [12] K. Kucharska, M. Pilz, K. Bielec, T. Kalwarczyk, P. Kuźma, R. Hołyst, Two intercalation mechanisms of oxazole yellow dimer (YOYO-1) into DNA, Mol. 26 (2021) 3748, http://dx.doi.org/10.3390/molecules26123748.
- [13] K. Bielec, A. Kowalski, G. Bubak, E. Witkowska Nery, R. Hołyst, Ion complexation explains orders of magnitude changes in the equilibrium constant of biochemical reactions in buffers crowded by nonionic compounds, J. Phys. Chem. Lett. 13 (2021) 112–117, http://dx.doi.org/10.1021/acs.jpclett.1c03596.
- [14] P.M. Korczyk, L. Derzsi, S. Jakieła, P. Garstecki, Microfluidic traps for hard-wired operations on droplets, Lab Chip 13 (2013) 4096–4102, http://dx.doi.org/10. 1039/C3I/C50347J
- [15] D. Zaremba, S. Błoński, P.M. Korczyk, Concentration on demand: A microfluidic system for precise adjustment of the content of single droplets, Chem. Eng. J. 430 (2022) 132935, http://dx.doi.org/10.1016/j.cej.2021.132935.
- [16] A. Kowalski, K. Bielec, G. Bubak, P.J. Żuk, M. Czajkowski, V. Sashuk, W.T.S. Huck, J.M. Antosiewicz, R. Hołyst, Effective screening of Coulomb repulsions in water accelerates reactions of like-charged compounds by orders of magnitude, Nat. Commun. 13 (2022) 6451, http://dx.doi.org/10.1038/s41467-022-34182-z.
- [17] D. Linke, Detergents: An overview, in: R.R. Burgess, M.P. Deutscher (Eds.), Guide to Protein Purification, Second Edition, in: Methods Enzymol., vol. 463, Academic Press, San Diego, 2009, pp. 603–617, http://dx.doi.org/10.1016/S0076-6879(09) 63034-2.
- [18] K. Makuch, R. Hołyst, T. Kalwarczyk, P. Garstecki, J.F. Brady, Diffusion and flow in complex liquids, Soft Matter 16 (2020) 114–124, http://dx.doi.org/10.1039/ C9SM01119F.
- [19] T. Kalwarczyk, K. Sozanski, A. Ochab-Marcinek, J. Szymanski, M. Tabaka, S. Hou, R. Hołyst, Motion of nanoprobes in complex liquids within the framework of the length-scale dependent viscosity model, Adv. Colloid Interface Sci. 223 (2015) 55–63, http://dx.doi.org/10.1016/j.cis.2015.06.007.
- [20] K. Bielec, K. Sozanski, M. Seynen, Z. Dziekan, P.R. ten Wolde, R. Hołyst, Kinetics and equilibrium constants of oligonucleotides at low concentrations: Hybridization and melting study, Phys. Chem. Chem. Phys. 21 (2019) 10798–10807, http://dx.doi.org/10.1039/C9CP01295H.
- [21] N.T.S. De Costa, J.M. Heemstra, Evaluating the effect of ionic strength on duplex stability for PNA having negatively or positively charged side chains, PLoS One 8 (2013) e58670, http://dx.doi.org/10.1371/journal.pone.0058670.
- [22] A.M. Smith, A.A. Lee, S. Perkin, The electrostatic screening length in concentrated electrolytes increases with concentration, J. Phys. Chem. Lett. 7 (2016) 2157–2163, http://dx.doi.org/10.1021/acs.jpclett.6b00867.
- [23] C.S. Swenson, H.H. Lackey, E.J. Reece, J.M. Harris, J.M. Heemstra, E.M. Peterson, Evaluating the effect of ionic strength on PNA:DNA duplex formation kinetics, RSC Chem. Biol. 2 (2021) 1249–1256, http://dx.doi.org/10.1039/D1CB00025J.
- [24] A.A. Almaqwashi, T. Paramanathan, I. Rouzina, M.C. Williams, Mechanisms of small molecule–DNA interactions probed by single-molecule force spectroscopy, Nucleic Acids Res. 44 (2016) 3971–3988, http://dx.doi.org/10.1093/ nar/skw237
- [25] G. Minotti, P. Menna, E. Salvatorelli, G. Cairo, L. Gianni, Anthracyclines: Molecular advances and pharmacologic developments in antitumor activity and cardiotoxicity, Pharmacol. Rev. 56 (2004) 185–229, http://dx.doi.org/10.1124/ pr.56.2.6.
- [26] C. Ozluer, H.E.S. Kara, In vitro DNA binding studies of anticancer drug idarubicin using spectroscopic techniques, J. Photochem. Photobiol. B 138 (2014) 36–42, http://dx.doi.org/10.1016/j.jphotobiol.2014.05.015.
- [27] S. Charak, R. Mehrotra, Structural investigation of idarubicin–DNA interaction: Spectroscopic and molecular docking study, Int. J. Biol. Macromol. 60 (2013) 213–218. http://dx.doi.org/10.1016/j.jibiomac.2013.05.027.
- [28] S. Charak, C.M. Srivastava, D. Kumar, L. Mittal, S. Asthana, R. Mehrotra, M. Shandilya, Beyond DNA interactions: Insights into idarubicin's binding dynamics with tRNA using spectroscopic and computational approaches, J. Photochem. Photobiol. B 266 (2025) 113147, http://dx.doi.org/10.1016/j.jphotobiol.2025.
- [29] D. Zaremba, S. Błoński, P.M. Korczyk, Integration of capillary-hydrodynamic logic circuitries for built-in control over multiple droplets in microfluidic networks, Lab Chip 21 (2021) 1771–1778, http://dx.doi.org/10.1039/ DOLC00900H.
- [30] J. Friend, L. Yeo, Fabrication of microfluidic devices using polydimethylsiloxane, Biomicrofluidics 4 (2010) 026502, http://dx.doi.org/10.1063/1.3259624.